

Atomistic simulations of the sliding friction of graphene flakes

Federico Bonelli¹, Nicola Manini¹, Emiliano Cadelano², and Luciano Colombo²

¹ Physics Department and INFN - University of Milan and European Theoretical Spectroscopy Facility
 Via Celoria 16, 20133 Milano, Italy

² Department of Physics, University of Cagliari and SLACS-INFN/CNR Sardinian Laboratory for Computational Materials Science
 Cittadella Universitaria, I-09042 Monserrato (Ca), Italy

April 2, 2008

Abstract. Using a tight-binding atomistic simulation, we simulate the recent atomic-force microscopy experiments probing the slipperiness of graphene flakes made slide against a graphite surface. Compared to previous theoretical models, where the flake was assumed to be geometrically perfect and rigid, while the substrate is represented by a static periodic potential, our fully-atomistic model includes quantum mechanics with the chemistry of bond breaking and bond formation, and the flexibility of the flake. These realistic features, include in particular the crucial role of the flake rotation in determining the static friction, in qualitative agreement with experimental observations.

PACS. 68.35.Af, 62.20.Qp, 81.05.Uw, 07.79.Sp

1 Introduction

The scanning tunneling microscope (STM) [1], and even more the atomic-force microscope (AFM) [2], have triggered perhaps the biggest wave of advances and discoveries ever in surface science and nanoscience. Experimental investigations of friction on the atomic scale have become possible by virtue of the friction force microscope (FFM). In a FFM experiment a sharp tip scans a sample surface with atomic precision, while lateral forces are recorded with a resolution that can reach the pN range. Since Mate *et al.* [3] investigated the nanoscale periodic frictional force map of a graphite surface using a tungsten tip, many studies have been conducted experimentally and theoretically. In recent works the Leiden group [4,5] has probed quantitatively the well known slipperiness of graphite, responsible for its excellent lubrication properties. Morita *et al.* [6] suggested that in FFM experiments on layered materials, such as MoS₂ or graphite, a flake, consisting of several hundred atoms in contact with the substrate, can attach to the tip. By controlling the relative angles of individual nanoflakes to achieve a suitable lattice mismatch, thus incommensurate contact [7], an almost frictionless sliding was demonstrated for dry and wearless tip-surface contact, a phenomenon known as superlubricity. Several experiments and calculations have been probing the effects of lattice mismatch on friction [8,9,10,11,12,13] showing that incommensuracy often prevents global ingrain-ing of large areas, thus attenuating the consequent strongly dis-sipative stick-slip motion. Theoretically, atomic-scale friction on ideal solid surfaces is often described by simple balls-and-springs models such as the Tomlinson model [14], where a single atom, or a more structured tip [15], is dragged through a spring along a static periodic potential energy surface. In the present work we implement a Tomlinson-like model of a sim-

ulated FFM experiment where dissipation of a finite graphene flake is driven along a graphite substrate, in a fully atomistic scheme based on a tight-binding (TB) force field. Compared to similar models in the literature [16,17,18,19], where the flake is assumed to be perfect and rigid and the substrate is represented by an analytically defined static periodic potential, our fully-atomistic TB simulation explores two realistic features, namely: (i) The flake-substrate interaction potential is not classical and contains quantum mechanics with the chemistry of bond breaking and bond formation. (ii) The flake is non-rigid, so that during its advancement it can deform and relax. In Sec. 2 we introduce the model implementation details. Section 3 reports the results obtained, in particular for the friction dependency on the flake size, the rotation angle relative to the substrate, and the applied load; we compare the results of the present model to experiment and to previous calculations. The final Sec. 4 discusses the results and the advantages and drawbacks of the present model.

2 The model

We describe the sliding by means of a generalized Tomlinson-like model similar to that of Ref. [17], but including the following features: (i) the interaction among all carbon atoms is realized in terms of the tight-binding scheme of Xu *et al.* [20], and (ii) the flake is not rigid but is allowed to deform and rotate while sliding. Interatomic forces are computed as customary in the TB scheme [21]; the hopping parameters and the pairwise repulsive potential term follow the scaling form given by Xu *et al.* [20]. All interatomic interactions vanish at a cutoff distance $r_c = 2.6 \text{ \AA}$. This distance sits in between the nearest-neighbor and the next-nearest-neighbor distances of

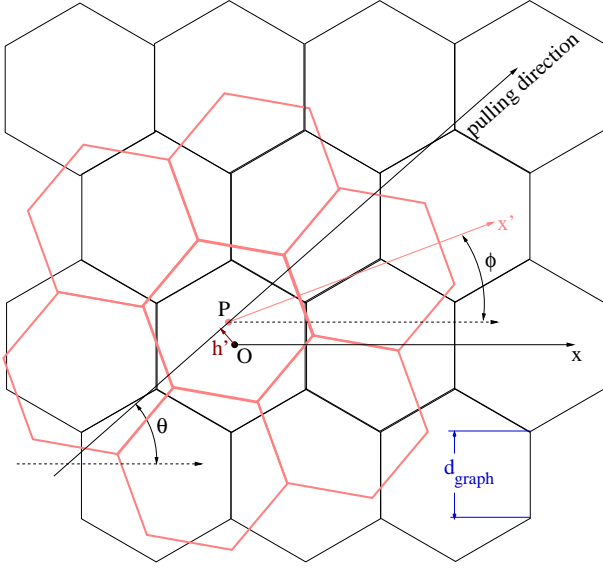


Fig. 1. (Color online) The definition of the angle ϕ measuring the initial rotation of the flake (thick, pink lines) with respect to the substrate honeycomb structure (thin, black lines). The pulling line is defined by its distance h' to the center of a substrate hexagon and the pulling angle θ . To take as a reference the AB stacking ($\phi = 0$), we define h' in terms of the parameter $h = h' + \frac{1}{2}d_{\text{graph}}$.

carbon atoms of the equilibrium sp^3 diamond structure, and of the sp^2 graphene plane. It is also shorter than the interlayer distance of graphite, which is as long as 3.35 \AA [22]. The present TB model has been applied successfully to investigate several low-dimensional carbon systems [23,24,25]. In particular, this parameterization reproduces the experimental equilibrium distance $d_{\text{graph}} = 1.4224 \text{ \AA}$ of the graphitic plane. To study friction, we use a model constituted by a graphene flake sliding over a single infinite rigid graphene sheet. The infiniteness of the substrate is simulated by repeating periodically a regular arrangement of N^{sub} atoms at positions $\mathbf{r}_i^{\text{sub}}$ in the $x-y$ plane. We consider a periodic rectangular supercell, containing as many carbon atoms as necessary for the flake not to interact with its periodic images.

We have studied three different regular hexagonal flakes composed of $N^{\text{fl}} = 24, 54$, and 96 atoms, respectively. Initially, the flake is rotated by an angle ϕ with respect to the substrate and translated horizontally to put its center of mass along a sliding line at a distance h' from the center of a substrate hexagon. As illustrated in Fig. 1, this line is oriented at an angle θ from the \hat{x} direction, which is defined by being parallel to the zig-zag direction of the honeycomb lattice. In our simulations we drag the flake along this pulling line and usually let the flake atoms relax in all directions (x, y and z), whereas the substrate remains completely rigid. The ϕ angle defines the stacking mismatch, which has a central importance for friction. Specific values of θ such as 0° and 30° define special pulling directions where the pulled flake encounters periodic corrugations, while aperiodic corrugations are experienced for generic θ angles. The range of interest of both angles θ and ϕ runs from 0° to 30° : outside this range we recover equivalent geometries.

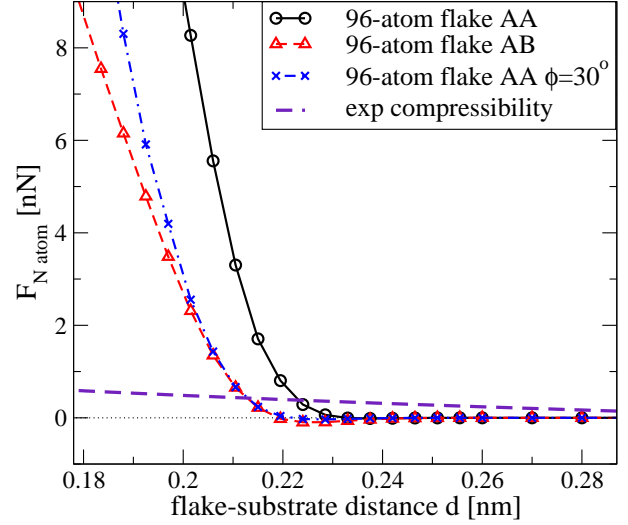


Fig. 2. (Color online) The computed normal force per atom $F_{N_{\text{atom}}}$ as a function of the fixed rigid flake-substrate distance d . The curves refer to different stackings (AA or eclipsed, AB and an incommensurate obtained starting from AB rotated by $\phi = 30^\circ$) for a 96-atom flake undeformed flake. The compression curve based on the low-pressure data of Ref. [26] is reported for comparison.

To simulate an AFM experiment we introduce a constant load F_N pushing the flake against the substrate along the vertical z direction and simulating the force applied by the actual tip. This load acts against the reaction forces produced by the interaction with the substrate. These forces are reported in Fig. 2 for a $N^{\text{fl}} = 96$ -atom flake in several configurations, and of course vanish beyond $r_c = 2.6 \text{ \AA}$, the TB interaction cutoff. For a distance $d \geq 0.18 \text{ nm}$, the load force per atom does not exceed 10 nN (a total load in the tens to few hundred nN for a flake composed by 10 to 10^2 atoms, corresponding to a load pressure $\approx 4 \text{ Mbar}$), which is a value practically accessible to FFM experiments [8,9,10]. A load per atom of 0.5 nN , with the selected force-field model, produces an approach distance near 0.21 nm , similar to the one obtained by assuming for the flake-substrate system the equilibrium interlayer separation of graphite (3.35 \AA) and the very soft c -axis compressibility [26], expressed as $d \ln c/dP = -2.8 \times 10^{-6} \text{ bar}^{-1}$. Note however that we apply this compressibility relation, also sketched in Fig. 2 for distances and pressures that go beyond its linear-response range of validity: in the region of close approach, $d \leq 0.22 \text{ nm}$, the actual force is likely to increase more rapidly, like in the TB model curves. We implement a Tomlinson-like dynamics with each flake atom coupled horizontally to a rigid “support” by elastic springs. The support is a set of ideal graphene-net points, which coincide with the initial flake atomic positions: $\mathbf{r}_i^{\text{sup}} = \mathbf{r}_i^{\text{fl}}(t = 0)$. This support is then translated rigidly parallel to the substrate. Its orientation is fixed once and for all by the angle ϕ . The support advances by steps of length δx along the direction defined by the pulling angle θ and lateral shift h' . After a few tests, we select an advancement step $\delta x = 0.0024 \text{ nm}$. After each advancement step relaxation, we evaluate and store the total spring energy and the total dragging force, defined as

follows:

$$E^{\text{spr}} = \frac{K}{2} \sum_{i=1}^{N^{\text{fl}}} \left(r_{xi}^{\text{fl}} - r_{xi}^{\text{sup}} \right)^2 + \left(r_{yi}^{\text{fl}} - r_{yi}^{\text{sup}} \right)^2 ; \quad (1)$$

$$\mathbf{F}_{\parallel}^{\text{spr}} = \sum_{i=1}^{N^{\text{fl}}} \mathbf{F}_{\parallel i}^{\text{spr}} , \quad (2)$$

$$\mathbf{F}_{\parallel i}^{\text{spr}} = -K \left(\mathbf{r}_i^{\text{fl}} - \mathbf{r}_i^{\text{sup}} \right)_{\parallel} , \quad (3)$$

where the \parallel symbol indicates the in-plane component. The component $F_{\parallel i}^{\text{spr}}$ of $\mathbf{F}_{\parallel i}^{\text{spr}}$ along the pulling direction equals the force needed to make the support advance, so that the work of this force equals $F_{\parallel i}^{\text{spr}} \delta x$, for an infinitesimal displacement in the pulling direction.

In an AFM experiment, the scanning tip speed is typically of the order of tens or hundreds nm/s, much slower than the fast dynamics of the flake. Assuming that the substrate temperature is fairly low, it is appropriate to consider a quasi-static motion of the flake as follows: after each advancement of the support, all flake atomic positions are made relax in all directions by damped dynamics¹ under the combined action of (i) the TB forces, (ii) the vertical load force F_N , and (iii) the horizontal spring forces that attract the flake atoms near the support points. When the stationary equilibrium position is reached (defined by no force component exceeding a threshold of 10^{-2} nN), the support moves one step further and the whole relaxation procedure is repeated until the support reaches the end of a pre-defined path. With the selected fairly small advancement step δx , each relaxation requires typically 10 to 200 MD steps. We consider a path of moderate length $d \approx 1$ nm divided into approximately 400 advancement steps. The spring elastic constant coupling the support and the flake in the x - y plane is a quite critical parameter of the present model. Softer springs allow the flake a greater freedom to translate, rotate, and deform, with better pinning to energetically favorable sites and more pronounced stick-slip motion and higher friction. Harder springs enforce a more stiff flake showing little or no stick-slip motion. The limit $K \rightarrow \infty$ matches the model by Verhoeven *et al.* [17]. The spring constant mimic the combined interaction between the flake and the tip and the elastic tip response. We suggest that a value

$$K = 0.5 \frac{\text{eV}}{\text{\AA}^2} \approx 8.01 \frac{\text{N}}{\text{m}} \quad (4)$$

corresponding to about 10% of the stretching stiffness of a carbon-carbon bond within a graphene layer should probably be fairly realistic. We also perform computations with softer ($K = 0.1 \text{ eV/\AA}^2$) and harder ($K_x = K_y = 2.5 \text{ eV/\AA}^2$) springs, as detailed in Sec. 3.

In our calculations, by convention, we estimate the static friction force F_{fric} along a given sliding path by the force level below which 95% of the spring force values $F_{\parallel}^{\text{spr}}$ encountered

¹ The advantage of damped dynamics with respect to a standard energy-minimization algorithm is that at each step it relaxes smoothly and predictably to the nearest local-minimum configuration. On the other hand, this algorithm is computationally less efficient than, e.g., a conjugated-gradient technique. Eventually we settle on a fairly fast converging damped dynamics with a time step $\delta t = 4$ fs.

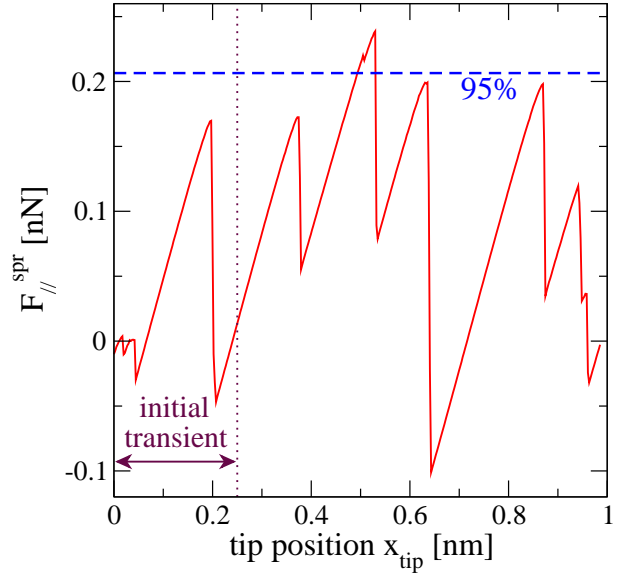


Fig. 3. (Color online) The spring total lateral force component $\mathbf{F}_{\parallel}^{\text{spr}}$ projected along the scan line, for a 24-atom flake dragged starting from an initial stacking AB along a pulling angle $\theta = 15^\circ$, and with a stacking angle $\phi = 30^\circ$. The spring constant is $K = 0.1 \text{ eV/\AA}^2$, the total load $F_N = 100$ nN. The 95% force level (dashed line) estimates the static friction force F_{fric} .

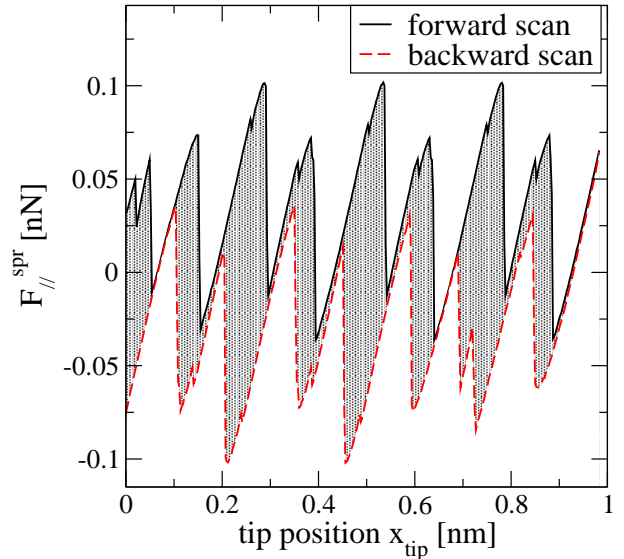


Fig. 4. (Color online) The dynamic-friction force is evaluated as the energy dissipated through a forward-backward scan (solid and dashed lines respectively). The shaded area between the two curves measures the energy dissipated by friction. The conditions are as follows: $N^{\text{fl}} = 24$, $F_N = 100$ nN, $\theta = 0^\circ$, $\phi = 0^\circ$, $K = 0.1 \text{ eV/\AA}^2$.

along the path (at the end of each relaxation, and excluding an initial transient) are found. This definition is illustrated in Fig. 3. The dynamic-friction force is defined in terms of the energy dissipated in a forward-backward loop. Figure 4 illustrates this concept: the component of the spring force parallel to the advancement direction shows a clear hysteric behavior in a forward-backward scan. The shaded area enclosed be-

tween the two curves measures the energy E_{fric} dissipated by friction, and is clearly related to the stick-slip events. The average dynamical friction force $F_{\text{fric}}^{\text{dynamic}} = E_{\text{fric}}/d \approx 0.325$ nN is of course smaller than the static friction force $F_{\text{fric}} \approx 0.9$ nN evaluated according to the 95% protocol described above. In the following we will focus on the static friction force F_{fric} , which is cheaper to compute and eventually of the same order as $F_{\text{fric}}^{\text{dynamic}}$. As the flake advances along its path, it deforms and rotates around its center of mass. In particular, to understand the evolution of the static friction force, it is useful to track the flake instantaneous stacking angle ϕ_A , which generally differs from the fixed support angle ϕ . At each relaxed configuration, we calculate ϕ_A as an average over all flake atoms i , of a sine projection obtained as the length of the vector product of two vectors in the horizontal xy plane: \mathbf{R}_i^{cm} , joining the flake center of mass to the i -th flake atom, and the corresponding vector $\mathbf{R}_i^{0\text{cm}}$ computed for the unrotated $\phi = 0^\circ$ support. Explicitly:

$$\phi_A = \arcsin\left(\sum_i \frac{R_i^{\text{cm}y} R_i^{0\text{cm}x} - R_i^{\text{cm}x} R_i^{0\text{cm}y}}{N^{\text{fl}} |\mathbf{R}_i^{\text{cm}}| |\mathbf{R}_i^{0\text{cm}}|}\right). \quad (5)$$

3 Results

We analyze the friction force dependence on several physical parameters, namely the pulling angle θ , stacking angle ϕ , applied load, flake size and position of the scan-line. Experimentally, the number of flake atoms, estimated in the order of 100, is not well determined, while the total applied load and the total force acting on the flake are under control in the FFM. For ease of comparison with experiments, our discussion shall always deal with total quantities, i.e. summed over the flake atoms.

3.1 Relaxation to equilibrium

Optimally stacked configurations are important in providing the most efficient sticking points during a friction sliding experiment. Figs. 5, 6, and 7 report typical such relaxed configurations for 24-, 54- and 96-atom flakes respectively, obtained under the action of a total load of 100 nN, and with no spring connection to a support ($K = 0$). The relaxed configuration (up to a symmetry rotation/translation) depends only moderately on the starting stacking, unless the initial stacking angle is strongly incommensurate. The average vertical flake-substrate separation is 0.192 nm. The equilibrium configuration tends to arrange the flake so as to minimize the number of flake atoms stacked on top of a substrate atom: indeed Fig. 2 shows that the eclipsed “AA” stacking produces the strongest repulsive force at the same distance. Geometrically different non-optimal configurations are characterized by typical excess total energies of 1 eV or less.

3.2 The stick-slip movement

We come now to the actual simulation of sliding friction: to start with, Fig. 8 displays the pulling force $F_{\parallel}^{\text{spr}}$ measured along two sliding paths of different commensurability nature: $\theta = 0^\circ$

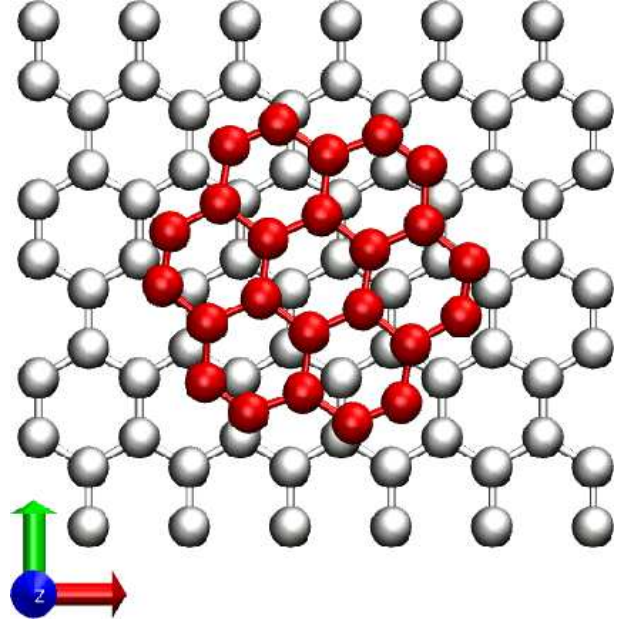


Fig. 5. (Color online) The relaxed configuration of the 24-atom flake. Static substrate atoms are clear (white), flake atoms are dark (red).

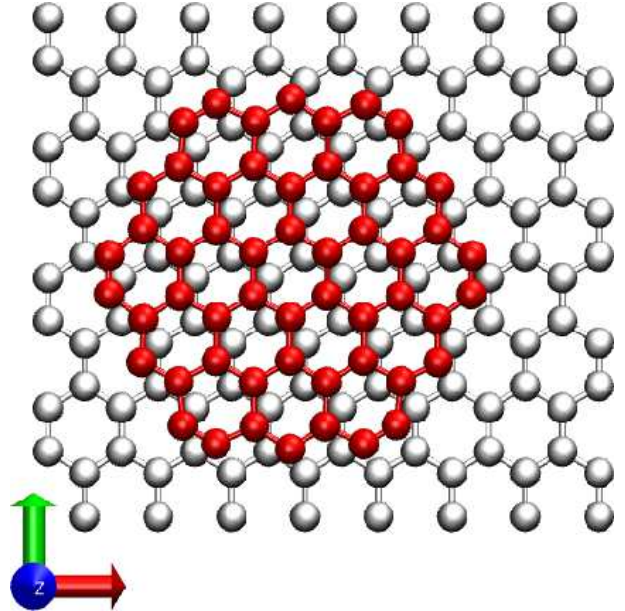


Fig. 6. (Color online) The relaxed configuration of the 54-atom flake. Static substrate atoms are clear (white), flake atoms are dark (red).

(periodic) and $\theta = 15^\circ$ (aperiodic). As expected, the regular stick-slip pattern of the $\theta = 0^\circ$ path is replaced by an irregular dependency in the $\theta = 15^\circ$ trajectory. The initial part of the $\theta = 0^\circ$ trajectory is not periodic because of the usual startup transient behavior: the first 0.2 nm are omitted from the calculation of the friction force, as discussed above.

The stick-slip motion and the role of the spring stiffness is understood even better by comparing other physical quantities with $F_{\parallel}^{\text{spr}}$. In particular, Fig. 9 displays the internal energy of the flake-substrate interaction, the displacement of the flake center of mass along the pulling direction, and the actual stack-

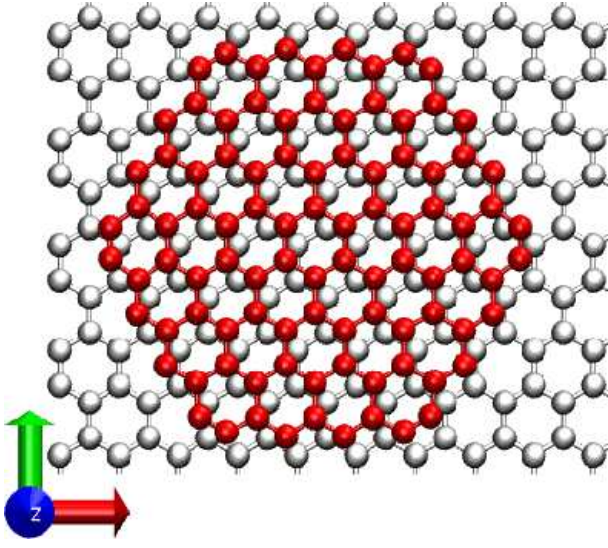


Fig. 7. (Color online) The relaxed configuration of the 96-atom flake. Static substrate atoms are clear (white), flake atoms are dark (red).

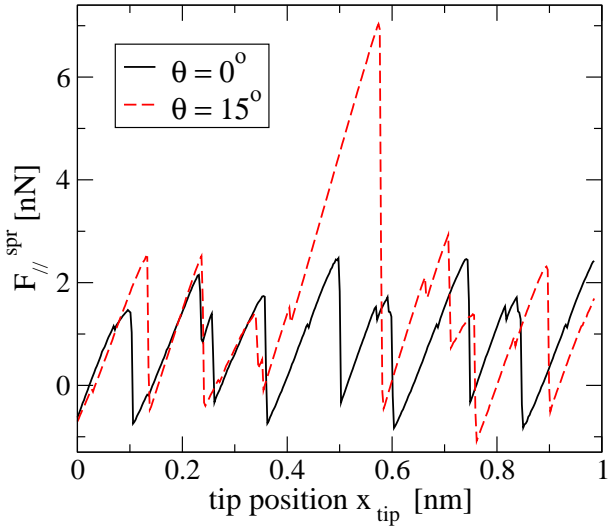


Fig. 8. (Color online) The component of the springs force $F_{||}^{\text{spr}}$ in the dragging direction as a function of the support advancement distance x_{tip} for two different pulling directions: $\theta = 0^\circ$ (solid) and $\theta = 15^\circ$ (dashed). The simulation involves a 24 atom flake with total applied load of 100 nN, support stacking angle $\phi = 0^\circ$ and spring constant $K = 0.1 \text{ eV/\AA}^2$.

ing angle ϕ_A . We focus initially on the solid curves, obtained in a simulation based on soft springs with $K = 0.1 \text{ eV/\AA}^2$. After the initial transient, where the flake explores once a configuration with a negative ϕ_A , it then jumps back and forth between two kinds of sticking configurations: the most favorable one characterized by $\phi_A \approx 4^\circ$, and another one, at 0.1 to 0.2 eV higher energy, near $\phi_A \approx 0^\circ$. These stick-slip jumps overcome energy barriers whose heights are of order 0.2 to 0.3 eV. This energy amplitude sets the temperature range of validity of the present zero-temperature calculations to a few hundred Kelvin: when thermally-activated slips through energy barriers do not have enough time to occur, i.e. for a not-too-small tip advancement speed [27,28], these slips are unlikely and our estimates

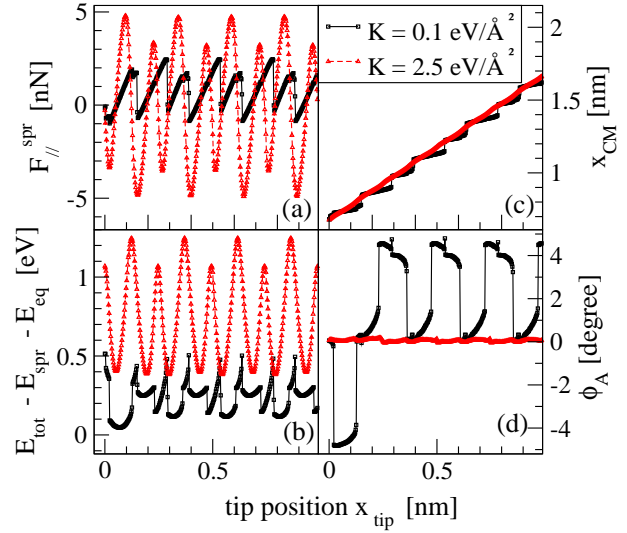


Fig. 9. (Color online) Several physical quantities plotted as functions of the support position x_{tip} : (a) the parallel component of the springs lateral force $F_{||}^{\text{spr}}$, (b) the flake excess energy $E_{\text{tot}} - E_{\text{spr}} - E_{\text{eq}}$, (c) the flake center-of-mass advancement x_{CM} along the pulling direction, and (d) the flake instantaneous rotation angle ϕ_A relative to the substrate. Two different values of the spring constant are compared: soft, $K = 0.1 \text{ eV/\AA}^2$ (solid, squares), and hard, $K = 2.5 \text{ eV/\AA}^2$ (dashed, triangles). These simulations involve $N^{\text{fl}} = 24$, $F_N = 100 \text{ nN}$, $\theta = 0^\circ$, and $\phi = 0^\circ$.

of friction should be fairly reliable. Stick-slip events occur with correlated jumps in the spring force, flake excess energy, flake position, and stacking angle. The very different dashed curves show that stiff springs (with $K = 2.5 \text{ eV/\AA}^2$) produce a much stronger and more rigid binding of the flake to the rigid support. Accordingly, such an unrealistically rigid coupling suppresses the stick-slip behavior: both the advancement, shown in Fig. 9(c), and the spring force, Fig. 9(a), become smooth and jump-less. Despite the suppression of stick-slip, we observe higher force peaks for the stiffer springs, thus indicating a higher static friction than for the softer springs. This is due to the flake being forced to cross high potential-energy barriers, Fig. 9(b), with little or no possibility to avoid them by (i) shifting away from the pulling direction, (ii) deforming, and (iii) “rotating around” ($|\phi_A| < 0.2^\circ$). A similar behavior is observed also in different geometries. The spring strength tuning the coupling between the flake and the AFM tip plays therefore an important role in the model calculations. We checked that up to spring constants of an intermediate value ($K = 0.5 \text{ eV/\AA}^2$) our model still performs a stick-slip motion similar to the one found in experiment [4] (where the cantilever harmonic constants values was estimated $K \approx 0.36 \text{ eV/\AA}^2$), especially in the fully commensurate $\phi = 0^\circ$ stacking.

3.3 Flake-size effects

Figure 10 compares the frictional behavior of flakes of different size, showing that friction tends to decrease with increasing flake size. In detail, the static friction force of the 3 flakes is $F_{\text{fric}} = 2.99 \text{ nN}$, 1.38 nN , and 1.24 nN for the 24, 54, and 96-atom flakes respectively. This decrease is not surprising, since

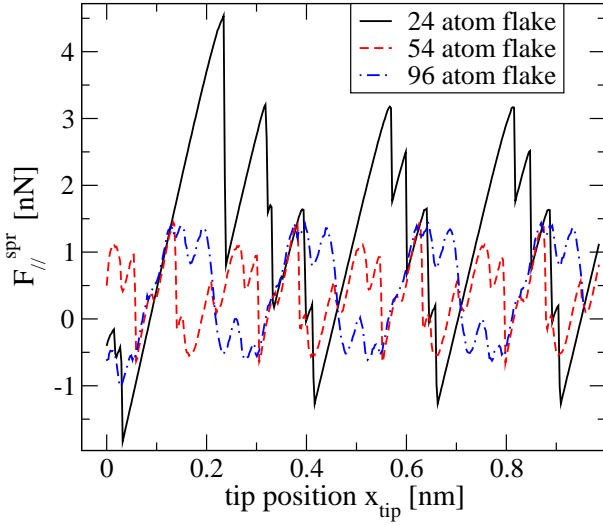


Fig. 10. (Color online) The parallel component of springs lateral force, $F_{||}^{\text{spr}}$, as a function of the support position x_{tip} for three flake sizes: 24-atom flake (solid), 54-atom flake atoms (dashed), and 96-atom flake atoms (dot-dashed). The three simulations involve a total applied load $F_N = 100$ nN, $\theta = 0^\circ$, $\phi = 30^\circ$, and soft springs constants $K = 0.1$ eV/Å².

the more reactive atoms at the flake boundary tend to bend down toward the substrate. As a result, friction is dominated by these boundary atoms, which amount to 75% of the 24-atom flake but only 44% of the 96-atom flake. Moreover, the 96-atom flake advances continuously, and shows no stick-slip, at variance with the 24-atom and 54-atom flakes. This difference is due to a reduced rotational freedom of the 96-atom flake, due to coupling to the support acting at a larger distance from the flake center. The flake rotational freedom, i.e. the angular range of ϕ_A explored around ϕ , does represent a key issue in the friction physics of carbon flakes sliding over a graphite surface, as pointed out by Filippov *et al.* [19].

In the framework of our model, with each atom tied to the moving support by an individual spring, the flake can both shift normally to the pulling direction and rotate around its center of mass: these degrees of freedom (and, more weakly, the possibility of the flake to distort) affect friction in two very different manners depending on the contact being commensurate or incommensurate. When the flake is pulled at a commensurate stacking, e.g. $\phi = 0^\circ$, it encounters high potential-energy barriers thus high friction: the combined possibility of rotations and lateral shifts allows the flake to dribble the high barriers through local changes of trajectory. The first effect of flake shifts and rotations is then to reduce the friction of highly commensurate contacts. In contrast, when the flake slides with an incommensurate stacking, e.g. $\phi = 15^\circ$, it does not encounter high-energy barriers nor efficiently binding configurations, thus producing a low-friction motion. However rotations and shifts allow the flake to locate deeper energy wells (both moving apart from the pulling direction and rotating so as to explore different stacking configurations), where the flake can stick, eventually providing sizeable friction. This second effect is therefore to raise the friction for incommensurate contacts and eventually destroy superlubricity, as was observed and discussed by Filippov *et al.* [19].

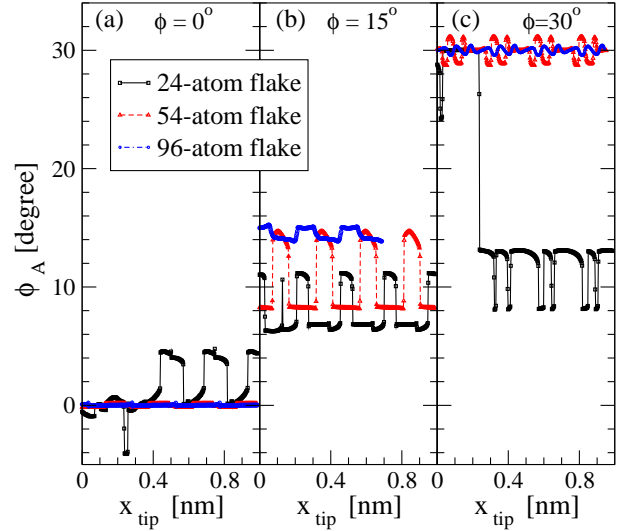


Fig. 11. (Color online) The instantaneous rotation angle ϕ_A as a function of the support position x_{tip} for three values of the support stacking angle: (a) $\phi = 0^\circ$, (b) $\phi = 15^\circ$, and (c) $\phi = 30^\circ$. Three flake sizes are considered: $N^{\text{fl}} = 24$ (black solid line), $N^{\text{fl}} = 54$ (red dashed line) and $N^{\text{fl}} = 96$ (blue dot-dashed line). Simulations are carried out with total applied load of 100 nN, pulling angle $\theta = 0^\circ$ and soft springs $K = 0.1$ eV/Å².

In our simple model the single parameter K tunes the flake rotational freedom and that of shifting perpendicular to the pulling direction. However, while its effect on the translational freedom is independent of size, the rotational freedom does depend on the larger torque that springs of the same stiffness exert on flake atoms more remote from the flake center, as is also to be expected for a flake sticking to a not too sharp AFM tip.

This point shows clearly in Fig. 11, which displays the evolution of the actual rotation angle ϕ_A along the scanline, for three different support stacking angles and three different flake sizes: $N^{\text{fl}} = 24, 54$, and 96 . Rotational fluctuations decrease as the flake size increases. Indeed significant systematic deviations of ϕ_A from ϕ are apparent in many cases, especially $N^{\text{fl}} = 24$. In particular, the small 24-atom flake for $\phi = 30^\circ$ rotates all the way to $\phi_A \leq 10^\circ$, thus displaying angular oscillations in excess of 15° , for an average angle $\langle \phi_A \rangle \approx 16^\circ$, very different from ϕ . When plotting the dependence of friction force F_{fric} on the stacking angle, it will make more sense to use, instead of the initial stacking angle ϕ , the average flake rotation angle $\langle \phi_A \rangle$, although even this indicator does not account properly for rotational fluctuations. This large rotational freedom, for hard springs, is almost completely frozen: in that case the largest rotational fluctuation we observe is as little as $\approx 3^\circ$ for $N^{\text{fl}} = 24$ and $\phi = 15^\circ$.

As for lateral shifts, for soft springs $K = 0.1$ eV/Å² we observe shifts perpendicular to the pulling line of the order of 1 Å, depicted in Fig. 12 which displays the actual path followed by the center of mass of a 24-atom flake pulled by the support along a $\theta = 0^\circ$ scanline. Note that, similarly to rotational fluctuations, the incommensurate stacking $\phi = 30^\circ$ yields larger lateral shifts than the commensurate stacking $\phi = 0^\circ$. With hard springs the possibility of the flake to perform lateral shifts is strongly reduced, so that the actual trajectory of the

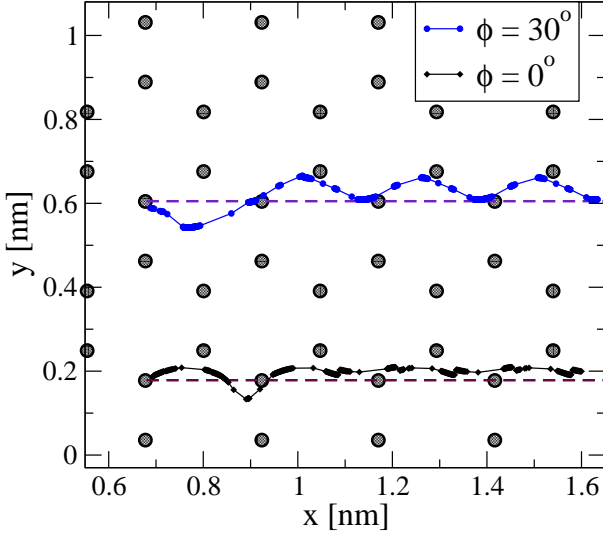


Fig. 12. (Color online) Subsequent points marking the trajectories of the center of mass of a 24-atom flake in the x - y plane for $\phi = 30^\circ$ (incommensurate stacking, blue circles) and for $\phi = 0^\circ$ (commensurate stacking, black diamonds) at the end of each relaxation cycle. The dashed lines represent the support scanlines ($\theta = 0^\circ$); large circles represent the substrate atomic positions. The simulations are the soft-spring ones of Fig. 9.

flake center of mass remains very close to the support scanline. For example, springs of $K = 2.5 \text{ eV/\AA}^2$ yield perpendicular shifts $\leq 0.2 \text{ \AA}$ along the same trajectory. The rotational freedom plus the lateral shifts of the flake can lead to effectively commensurate contacts even for an incommensurate stacking, thus explaining the deep energy valleys of the stick-slip motion pattern of Fig. 9b, eventually responsible for the stick-slip motion demonstrated by the lateral force patterns of Fig. 9a. For hard springs constants, locking into deep energy minima does not occur, but at the same time the flake is driven into highly repulsive geometries which it cannot dribble. This leads to higher force peaks, and eventually to a larger static friction.

3.4 Angular dependence of friction

As a reference benchmark we consider a nearly rigid flake model, where atoms are allowed to relax only in the z direction, corresponding to the $K \rightarrow \infty$ limit of the model studied until here, and comparing directly to the model used by Verhoeven *et al.* [17]. The complete suppression of angular fluctuations should produce an extremely sharp angular dependency of the friction force.

Figure 13 shows the computed static friction force as a function of the fixed stacking angle ϕ for different flakes. We note that friction decreases with the ϕ angle, showing a maximum peak centered at $\phi = 0^\circ$, similar to the outcome of previous model calculation [17]. As shown by experiments [4,5], friction is maximum at an highly commensurate contact ($\phi = 0^\circ$) and decreases rapidly as the flake rotates to incommensurate stackings. The friction peak is sharper for wider flakes. The sharpest peak for the 96-atom flake is similar to the one exhibited by the rigid model of Ref. [17]. F_{fric} decreases by nearly

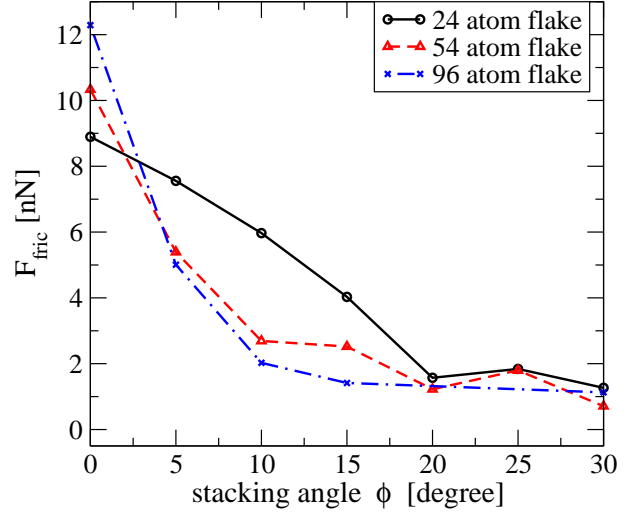


Fig. 13. (Color online) Friction force F_{fric} as a function of the fixed stacking angle ϕ for three different flake sizes: 24 atoms (black solid line), 54 atoms (red dashed line) and 96 atoms (blue dot-dashed line). The simulations are carried out with pulling angle $\theta = 0^\circ$ and total applied load of 100 nN. Flake atoms are allowed to relax only along z direction.

one order of magnitude from the high-friction $\phi = 0^\circ$ commensurate angle to the low-friction $\phi \simeq 30^\circ$ incommensurate one. This drop is smaller than was found by experiment [4], where it exceeded significantly one order of magnitude. Also the absolute values of friction are systematically larger than experiment. Experiment shows friction peak values near 0.2 nN, while the present model yields a peak value of order 10 nN, 50 times larger. This difference is even larger in the “superlubric” region near $\phi = 30^\circ$. These differences are to be ascribed to the larger load, the adopted short-ranged TB parameterization, and the neglect of thermal fluctuations, as discussed below.

The rigid-flake models, studied here and in previous work [4] do not look not especially realistic, since in practice a carbon flake does deform, shift and rotate while interacting with the graphite substrate and the AFM tip. Figure 14 reports the dependence of friction force F_{fric} on the average rotation angle $\langle \phi_A \rangle$, for a flake whose atoms are allowed to relax in all directions, for soft spring constants $K = 0.1 \text{ eV/\AA}^2$. In all calculations except those of 96-atom flake we use the same angles $\phi = 0^\circ, 5^\circ, 10^\circ, 15^\circ, 20^\circ, 25^\circ$ and 30° , but the possibility of flake rotations allowed by the soft springs produces significantly different effective average angles $\langle \phi_A \rangle$, especially for the 24-atom flake. Not surprisingly, with its vast rotational freedom, the 24-atom flake displays an almost ϕ -independent, constant friction. For such a small flake with soft springs, rotations and shifts are so effective to hinder the possibility to observe any reliable ϕ -dependency of F_{fric} . The 54-atom flake and, more clearly, the 96-atom flake show average angles nearer to the support values, with smaller-amplitude fluctuations, and therefore display a friction curve behavior with a peak at $\langle \phi_A \rangle \simeq 0^\circ$, fairly similar to the one obtained in the semi-rigid case and observed in experiment, and with smaller friction at incommensurate angles. These results suggest that when the FFM tip happens to bind to a graphene flake constituted by substantially less than

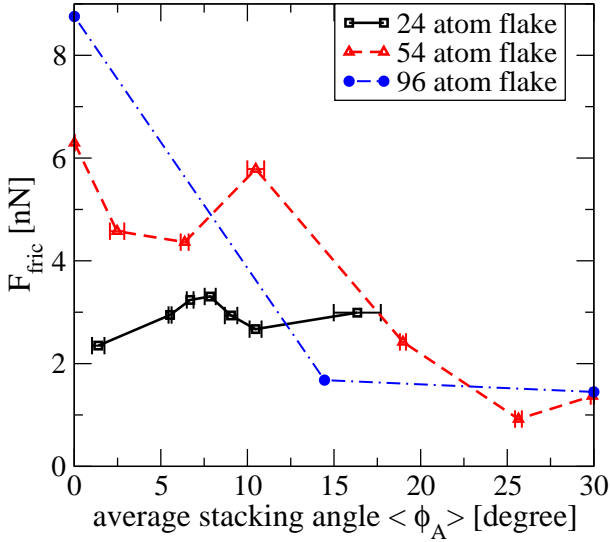


Fig. 14. (Color online) The friction force F_{fric} as a function of the average rotation angle $\langle \phi_A \rangle$ for three different flake sizes: 24 atoms (black solid line), 54 atoms (red dashed line) and 96 atoms (blue points). Simulations involve a pulling angle $\theta = 0^\circ$, total applied load of 100 nN and soft springs constants $K = 0.1 \text{ eV/\AA}^2$.

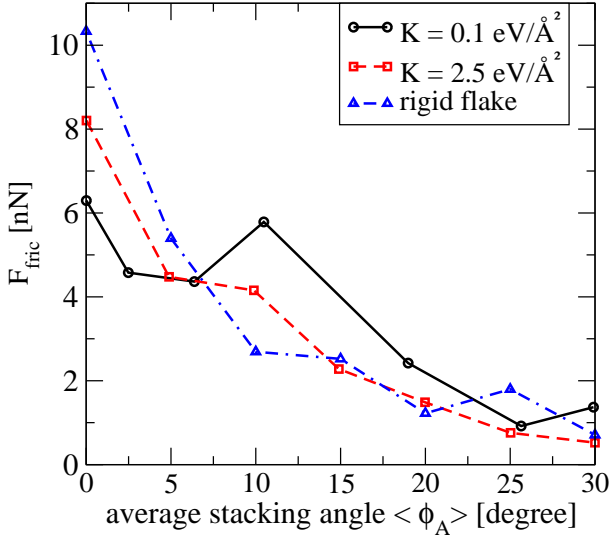


Fig. 15. (Color online) Comparison of the friction force dependence on the average rotation angle $\langle \phi_A \rangle$ for a 54-atom flake for two values of springs strength: soft $K = 0.1 \text{ eV/\AA}^2$ (black solid line) and hard $K = 2.5 \text{ eV/\AA}^2$ (red dashed line), plus the semi-rigid case (blue dot-dashed line). Simulations involve a pulling angle $\theta = 0^\circ$, total applied load of 100 nN.

approximately 10^2 atoms, no clear angular dependency and no superlubric regimes are observed.

Figure 15 summarizes the effect of increasing the rigidity of the springs on the friction dependency on $\langle \phi_A \rangle$: the friction peak at a commensurate arrangement becomes sharper and sharper as the spring rigidity increases. At variance with the radical changes in $\langle \phi_A \rangle$ dependency of the 24-atom flake as a function of the spring constant, for the 54-atom flake the shift-rotational effects become comparably less important, suggest-

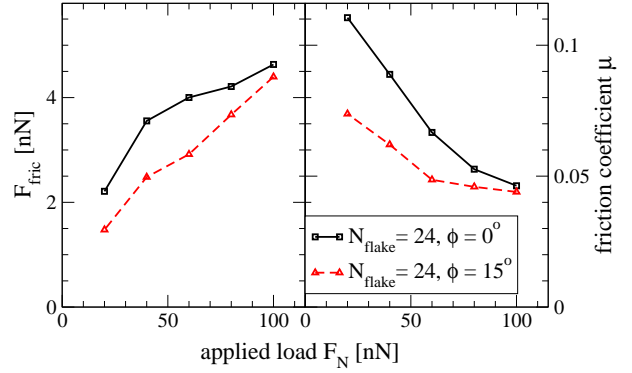


Fig. 16. (Color online) Nonlinear dependency of (a) the friction force and (b) the friction coefficient $\mu = F_{\text{fric}}/F_N$ on the total applied load F_N , for a commensurate contact ($\phi = 0^\circ$, black solid line) and an incommensurate contact ($\phi = 15^\circ$, red dashed line) of the 24-atom flake. Simulations are carried out for pulling angle $\theta = 0^\circ$ and rigid springs, $K = 2.5 \text{ eV/\AA}^2$.

ing that for realistically large flakes in excess of one hundred atoms, the precise value of the spring stiffness should become irrelevant, as long as it remains in the $\lesssim 1 \text{ eV/\AA}^2$ region.

3.5 Load dependency

We come now to study the dependence of the friction force F_{fric} on the applied load F_N , exploring a range 20 to 100 nN, matching typical experiment values [4,29]. Figure 16 shows the dependence of the friction force F_{fric} and coefficient $\mu \equiv F_{\text{fric}}/F_N$ on the applied load. Hard springs are selected to reduce the flake shift-rotational effects, in order to focus on the load dependence of friction and simpler comparison with earlier results. Friction increases with load, but significant deviations from the linear Coulomb law are observed, especially for commensurate stacking $\phi = 0^\circ$. Observe that experiment found an even weaker dependency of the friction force on load [4]. Although the data do not point clearly in the direction of a power-law behavior $F_{\text{fric}} \propto F_N^\alpha$, it is clear that if any such law was to be estimated, it would have $\alpha < 1$. This is at variance with previous findings for a sharp undeformable tip-surface contact [18], and with recent studies of the sliding of hydrogen-passivated carbon [30]. The resulting static friction coefficient approaches the standard macroscopic value [31] of graphite-graphite contact, $\mu = 0.1$, while much smaller values are found in the single-crystal FFM experiments addressed by the present model. Regardless of the applied load, the flake-substrate distance being smaller in the model than in real life produces larger absolute values of friction, and this overestimation is particularly severe at small load.

3.6 Scanline dependency

We investigate the dependence of the friction force versus stacking angle on the actual scanline followed by the support. Changing scanline determines a different potential profile seen by the flake, thus modifying the frictional behavior [18]. Figure 17 reports the friction angular dependency for three equally spaced

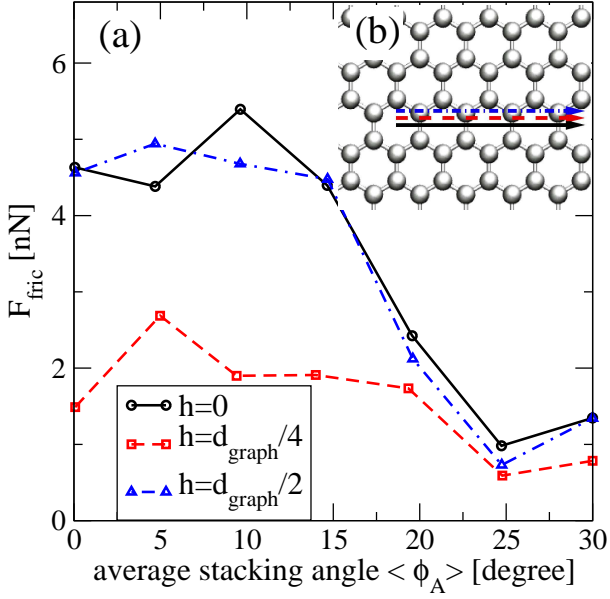


Fig. 17. (Color online) (a) Friction force F_{fric} as a function of the average stacking angle $\langle \phi_A \rangle$ for three different scanlines drawn in panel (b), defined by the three following initial stackings of the support over the substrate: AB (black solid), AB with a transverse shift $h = d_{\text{graph}}/4$ (red dashed) and AB with a transverse shift $h = d_{\text{graph}}/2$ (blue dot-dashed). The simulations involve a 24-atom flake, pulling angle $\theta = 0^\circ$, applied load $F_N = 100$ nN and hard springs of constants $K = 2.5$ eV/Å².

scanlines. We carry out simulations for hard springs $K = 2.5$ eV/Å² where scanline effects are the most visible, because of hindered lateral shifts. For the $h = 0$ and $h = d_{\text{graph}}/2$ scanlines we find a similar friction for all values of the stacking angle $\langle \phi_A \rangle$, while the $h = d_{\text{graph}}/4$ scanline shows systematically lower friction, especially for small ϕ . The reason is that for $\phi_A \approx 0$ along this special line each flake atom never hits any substrate atom directly on top, therefore effectively finding a significantly lower corrugation. In contrast along the two other scanlines, for $\phi = 0^\circ$ one half of flake atoms encounters periodically a substrate atom right below its trajectory, thus finding a high corrugation. Softer springs produce a much weaker dependence on the scanline: the flake takes advantage of its freedom to displace laterally, thus following low-corrugation lines (such as $h = d_{\text{graph}}/4$) even when the support pulls it along some nearby parallel line.

The scanlines of Fig. 17 involves $\theta = 0^\circ$, i.e. a pulling along the x direction, where the flake encounters periodic repetitions of the substrate potential. A different pulling angle affects directly this periodicity of the problem, in general leading to a nonperiodic profile. Figure 18 displays the friction force as a function of the pulling angle θ . Data are averaged over three different scanlines, defined by initial stacking with $h = 0$, $h = d_{\text{graph}}/4$ and $h = d_{\text{graph}}/2$. Like in previous calculations [17], we find a minimum friction for pulling angle $\theta = 0^\circ$, followed by a fast growth in friction (until $\theta = 10^\circ$). We attribute the observed differences between our results and those by Verhoeven *et al.* to the different interaction models.

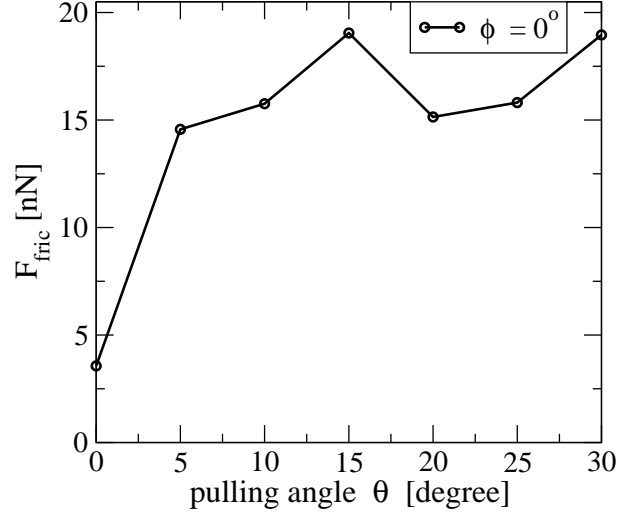


Fig. 18. Friction force F_{fric} as a function of the pulling angle θ . Static friction data are obtained by averaging three different scanlines, defined by initial stacking AB, AB shifted by $d_{\text{graph}}/4$ and AB shifted by $d_{\text{graph}}/2$ perpendicular to the pulling direction. Simulations involve a 24-atom flake with load of 100 nN, support stacking angle $\phi = 0^\circ$ and springs constants $K = 2.5$ eV/Å².

4 Discussion and conclusion

We find fair qualitative agreement between the results obtained by our TB atomistic model and the existing experimental data, with a few significant differences. Firstly, our calculations recover the stick-slip behavior of the lateral forces, characteristic of FFM sliding experiments. In particular, we find the correct qualitative dependence of stick-slip on the springs stiffness characterizing the cantilever-tip-flake coupling: soft springs allow for clean stick-slip behavior, while hard springs inhibit it. Our calculations also reproduce correctly the friction pattern as a function of the average stacking angle $\langle \phi_A \rangle$ especially as long as the rotational degree of freedom ϕ_A is quenched. We also find that for larger flakes, the fluctuation in ϕ_A are suppressed automatically anyway, due to the larger torque exerted by the springs connecting the flake to the tip. Accordingly, for flakes of sufficiently large size incommensurability produces significantly less friction, although the friction drop is smaller than in experiment. In the quantitative comparison between the experimental results and our model, we find static friction force F_{fric} and coefficient μ systematically at least one order of magnitude larger than experiment, this difference being especially significant in the incommensurate configurations where no proper superlubric regime is observed. These and other quantitative discrepancies are to be attributed to: (i) The reduced interlayer equilibrium distance, related to the small cut-off distance of the present TB parameterization, which is responsible for the increased energy corrugation experienced by our model flake with respect to real graphene on graphite. (ii) The extra reactivity of the isolated model graphene flake with respect to a real one, which is bonded to the AFM tip and thus somewhat passivated; accordingly, especially the atoms at the flake border, show a greater tendency to react with substrate atoms, thus increasing friction. (iii) The neglect of thermally-activated slips through energy barriers [27,28]: this neglect generates

an overestimation of friction especially where these barriers are lower, i.e. at incommensurate stackings. Indeed the current understanding [32] of the observed [4] superlubric sliding involves thermolubricity associated to a high attempt rate for overcoming the corrugation barriers due to the microscopic mass of the vibrating tip apex. If the experiment of Ref. [4] could be repeated at the much lower temperature of a few degree Kelvin, the observed friction values and dependency on the ϕ angle would probably look much more similar to the one obtained in the present model.

Calculations carried out with comparably soft springs and small flakes ($N_{\text{fl}} \leq 54$) show that the flake shift-rotational freedom increases friction for incommensurate stackings (by allowing the flake to explore deeper-bound minima) and decreases it for commensurate ones (by allowing the flake to dribble the top barriers): the result is a substantial flattening of the dependency of the friction static force F_{fric} on the stacking angle ϕ . Harder springs (e.g. $K = 2.5 \text{ eV/\AA}^2$) would suppress the flake freedom to rotate and shift laterally but are incompatible with the clear stick-slip behavior observed experimentally. These considerations confirm that the size of the flakes showing superlubric sliding in actual FFM experiments is large $N_{\text{fl}} \geq 96$. Many discrepancies with experiment would probably be disposed of, if a longer ranged interatomic interaction was employed, for example a TB model based on a longer cutoff [33]. This way, a much weaker flake-surface interaction would effectively correspond to comparably stronger tip-flake interaction, thus a significant hindering of rotations and translations even with a realistically weak tip-flake coupling $K \leq 0.5 \text{ eV/\AA}^2$. If accurate long-range C-C interactions up to distances of the order of 1 nm were present in the force field, one could even include substrate relaxation to study an even more realistic model. Such an improved model would however imply significantly larger computational workload, especially if thermal excitations were also included. Further research should also investigate the effect of the presence of structural defects in the flake or in the substrate, as proposed by Guo *et al.* [34], and the effect of flake shape.

Acknowledgments

We are grateful to J. Frenken and R. Buzio for useful discussion. We acknowledge financial support by the project MIUR-PON "CyberSar", and by the Italian National Research Council (CNR) through contract ESF/EUROCORES/FANAS/AFRI.

References

1. G. Binnig, H. Rohrer, Ch. Gerber, and E. Weibel, *Phys. Rev. Lett.* **49**, 57 (1982).
2. G. Binnig, C. F. Quate, and Ch. Gerber, *Phys. Rev. Lett.* **56**, 930 (1986).
3. C. M. Mate, G. M. McClelland, R. Erlandsson, and S. Chiang, *Phys. Rev. Lett.* **59**, 1942 (1987).
4. M. Dienwiebel, G. S. Verhoeven, N. Pradeep, J. W. M. Frenken, J. A. Heimberg, and H. W. Zandbergen, *Phys. Rev. Lett.* **92**, 126101 (2004).
5. M. Dienwiebel, N. Pradeep, G. S. Verhoeven, H. W. Zandbergen, and J. W. M. Frenken, *Surf. Sci.* **576**, 197 (2005).
6. S. Morita, F. Fujisawa, and Y. Sugawara, *Surf. Sci. Rep.* **23**, 1 (1996).
7. M. Hirano and K. Shinjo, *Phys. Rev. B* **41**, 11837 (1990).
8. S. Maier, O. Pfeiffer, Th. Glatzel, E. Meyer, T. Filleter, and R. Bennewitz, *Phys. Rev. B* **75**, 195408 (2007).
9. S. Maier, E. Gnecco, A. Baratoff, R. Bennewitz, and E. Meyer, *Phys. Rev. B* **78**, 045432 (2008).
10. T. Filleter, J. L. McChesney, A. Bostwick, E. Rotenberg, K. V. Emtsev, T. Seyller, K. Horn, and R. Bennewitz, *Phys. Rev. Lett.* **102**, 086102 (2009).
11. A. Vanossi, N. Manini, G. Divitini, G. E. Santoro, and E. Tosatti, *Phys. Rev. Lett.* **97**, 056101 (2006).
12. A. Vanossi, N. Manini, F. Caruso, G. E. Santoro, and E. Tosatti, *Phys. Rev. Lett.* **99**, 206101 (2007).
13. I. E. Castelli, N. Manini, R. Capozza, A. Vanossi, G. E. Santoro, and E. Tosatti, *J. Phys.: Condens. Matter* **20**, 354005 (2008).
14. G. A. Tomlinson, *Philos. Mag.* **7**, 905 (1929).
15. D. Tománek, W. Zhong, and H. Thomas, *Europhys. Lett.* **15**, 887 (1991).
16. M. R. Sorensen, K. W. Jacobsen, and P. Stolze, *Phys. Rev. B* **53**, 2101 (1996).
17. G. S. Verhoeven, M. Dienwiebel, and J. W. M. Frenken, *Phys. Rev. B* **70**, 165418 (2004).
18. C. Fusco and A. Fasolino, *Appl. Phys. Lett.* **84**, 699 (2004).
19. A. E. Filippov, M. Dienwiebel, J. W. M. Frenken, J. Klafter, and M. Urbakh, *Phys. Rev. Lett.* **100**, 046102 (2008).
20. C. H. Xu, C. Z. Wang, C. T. Chan, and K. M. Ho, *J. Phys.: Condens. Matter* **4**, 6047 (1992).
21. L. Colombo, *Rivista Nuovo Cimento* **28**, 1 (2005).
22. R. Zacharia, H. Ulbricht, and T. Hertel, *Phys. Rev. B* **69**, 155406 (2004).
23. A. Canning, G. Galli, and J. Kim, *Phys. Rev. Lett.* **78**, 4442 (1997).
24. Y. Yamaguchi, L. Colombo, P. Piseri, L. Ravagnan, and P. Milani, *Phys. Rev. B* **76**, 134119 (2007).
25. E. Cadelano, P. L. Palla, S. Giordano, and L. Colombo, submitted for publication.
26. M. L. Yeoman and D. A. Young, *J. Phys. C* **2**, 1742 (1969).
27. E. Riedo, E. Gnecco, R. Bennewitz, E. Meyer, and H. Brune, *Phys. Rev. Lett.* **91**, 084502 (2003).
28. E. Gnecco, R. Bennewitz, A. Socoliuc, and E. Meyer, *Wear* **254**, 859 (2003).
29. N. Sasaki, S. Watanabe, and M. Tsukada, *Phys. Rev. Lett.* **88**, 046106 (2002).
30. Y. Mo, K. T. Turner, and I. Szlufarska, *Nature* **457**, 1116 (2009).
31. D. R. Lide, *CRC Handbook of Chemistry and Physics* (CRC Press, Boca Raton, 1994), 15-40.
32. J. W. M. Frenken, *Friction and thermolubrication: thermal fluctuations and 'universal' behavior*, communication at the Conference "Physics of Tribology", Bad Honnef, 23-25 March 2009.
33. D. A. Papaconstantopoulos, M. J. Mehl, S. C. Erwin and M. R. Pederson, in *Tight-Binding Approach to Computational Materials Science*, P. Turchi, A. Gonis, and L. Colombo, eds., Material Research Society Proceedings **491**, 221 (1998).
34. Y. Guo, W. Guo, and C. Chen, *Phys. Rev. B* **76**, 155429 (2007).